Supporting information for

Scalable nanoimprint manufacturing of achromatic metalenses based on high-refractive-index and low-shrinkage photoresist

Shihan Rong[1,2,3,], Ze Yang[4,*], Lu Han[1,3], Yunxiao Cai[1,3], Qi'an Wang[1,3], Meng Wang[1,3], Cheng Li[1,3], Weiming Xu[1,2,3], Taha Sheheryar[5], Lingling Huang[4], Yongtian Wang[4], Nan Zhang[4,†], and Wanjiao Zhang[1,3,†]*

[1]School of Physical and Optoelectronic Engineering, Hangzhou Institute for Advanced Study, University of Chinese Academy of Sciences, Hangzhou 310024, China

[2]Key Laboratory of Space Active Opto-Electronics Technology, Shanghai Institute of Technical Physics, Chinese Academy of Sciences, Shanghai 200083, China

[3]University of Chinese Academy of Sciences, Beijing 100049, China

[4]Beijing Engineering Research Center of Mixed Reality and Advanced Display, School of Optics and Photonics, Beijing Institute of Technology, Beijing 100081, China

[5]Key Laboratory of In-Fiber Integrated Optics of Ministry of Education, College of Physics and Optoelectronics Engineering, Harbin Engineering University, Harbin 150001, Heilongjiang Province, China

*These authors contributed equally to this work.

†Correspondence to: Nan Zhang: nanzhang@bit.edu.cn, Wanjiao Zhang: zhangwanjiao@ucas.ac.cn

This file includes:

Supplementary Note 1: Performance comparison between this work and previously reported nanoimprint photoresists

Table S1 systematically compares the key properties of the nanoimprint photoresist used in this work with those of TiO_2 nanoparticle-doped nanoimprint photoresists reported in previous literature, including refractive index and curing volume shrinkage. Although pioneering studies in this field have achieved high refractive index of photoresists via nanoparticle doping, they generally suffer from a critical drawback: severe volume shrinkage of up to approximately 20% occurs during the ultraviolet curing process. This issue readily induces dimensional distortion of high-aspect-ratio nanostructures, ultimately leading to a significant discrepancy between the actual optical performance of metalenses and their theoretical design values. In contrast, the novel nanoimprint photoresist employed in this work not only maintains a broadband high refractive index of 1.92-1.97 in the visible light range, but also realizes ultra-low curing volume shrinkage. This can minimize the phase or group delay deviation caused by dimensional errors, providing reliable material support for the fabrication of achromatic metalenses.

Table S1. Comparison of the nanoimprint photoresist used in this work with previous reports

Work Author	Nanoparticle	Refractive Index	Shrinkage Rate
Gwanho Yoon[34]	TiO_2	1.94 (532 nm)	~20%
Vincent J. Einck[35]	TiO_2	1.9 (543 nm)	~20%
Our work	TiO_2	1.92-1.97 (visible spectrum)	⩽5.19%

Supplementary Note 2: Effect of silane-based additives on polymerization shrinkage of nanoimprint photoresist

To analyze the effects of silane and methacryl-functionalized silane additives on the shrinkage of the nanoimprint photoresist, we prepared two samples using the same grating master, with and without the additives, respectively, and characterized both samples by SEM. The results are shown in Figure S1. The height and width of the gratings were measured using ImageJ. Without additives, the NIL sample exhibits an average grating width of approximately 172 nm and an average height of approximately 248 nm; with the incorporation of the additives, the average grating width increases to approximately 241 nm and the average height to approximately 324 nm. As a result, the width increases by 69 nm (28.63%) and the height increases by 76 nm (23.46%) with the use of additives. These results demonstrate that silane-based additives significantly reduce the polymerization shrinkage of the photoresist.

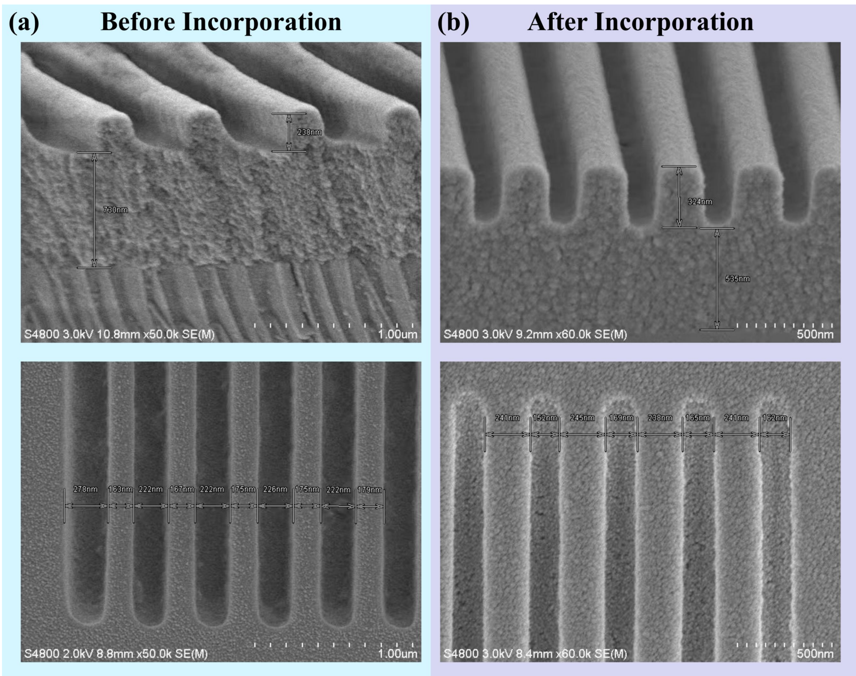

Figure S1. (a) SEM image of the grating sample without additives; (b) SEM image of the grating sample with additives.

Supplementary Note 3: Original ellipsometric test spectra

The refractive index and extinction coefficient of the nanoimprint photoresist were measured using an ellipsometer (RC2-XI, J.A. Woollam). Figure S2 shows the original ellipsometry test spectra. The parameters $\mathbf{\Psi}$ and $\mathbf{\Delta}$ in the figure are used to fit the optical constants. The Cauchy dispersion model is adopted for fitting:

$$\begin{cases} n(\lambda) = A + \dfrac{B}{\lambda^2} + \dfrac{C}{\lambda^4} \\ k = k_{amp}\, e^{E-E_{band}} \end{cases} \tag{S1}$$

A, B, C, k_{amp} and the exponential term are variable fitting parameters. They determine the dispersion of the refractive index and extinction coefficient.

The fitting results are A = 1.868 ± 0.001510; B = 0.01685 ± 0.00016224; C = 0.00072295 ± 2.7013E-5; k_{amp} = 0, with an exponential term of 2. The fitting root mean squared error (MSE) is 35.986. This proves the high reliability of the fitting results. The final n and k curves are shown in Figure 2b. In the 480-640 nm wavelength band, the nanoimprint photoresist shows a high refractive index (n = 1.92-1.97). Meanwhile, the extinction coefficient is 0, which means the nanoimprint photoresist has almost no light absorption.

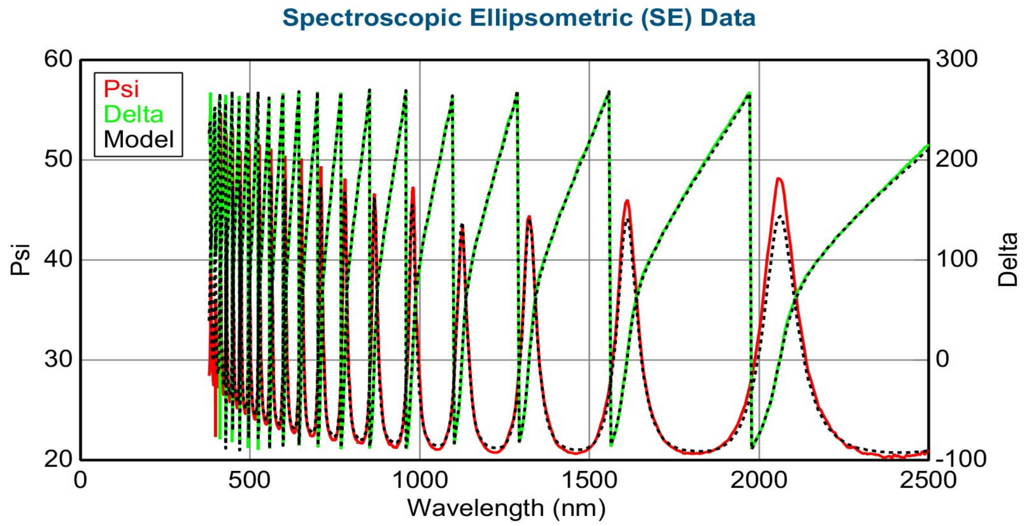

Figure S2. Original ellipsometric test spectra

Supplementary Note 4: Haze of the nanoimprint photoresist

This section presents the measured haze results. The haze was characterized using a UV-Vis-NIR spectrophotometer (Lambda1050+, PerkinElmer). As shown in Figure S3, the haze distribution in the wavelength range of 380-780 nm is displayed, with an average haze of only 0.38%, indicating that the nanoimprint photoresist exhibits extremely low optical scattering.

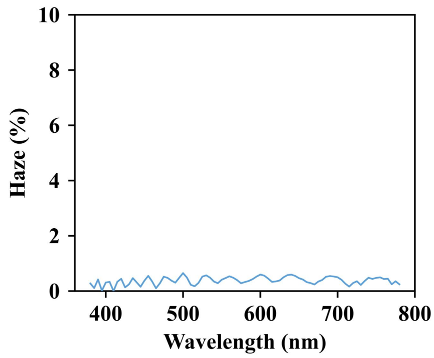

Figure S3. Haze of the nanoimprint photoresist

Supplementary Note 5: Phase and polarization conversion efficiency distributions of meta-atoms with varied dimensions

This section presents the phase distribution and polarization conversion efficiency distribution of meta-atoms with (**L**) and (**W**) ranging from 166-336 nm at **θ** = 0°, as shown in Figure S4.

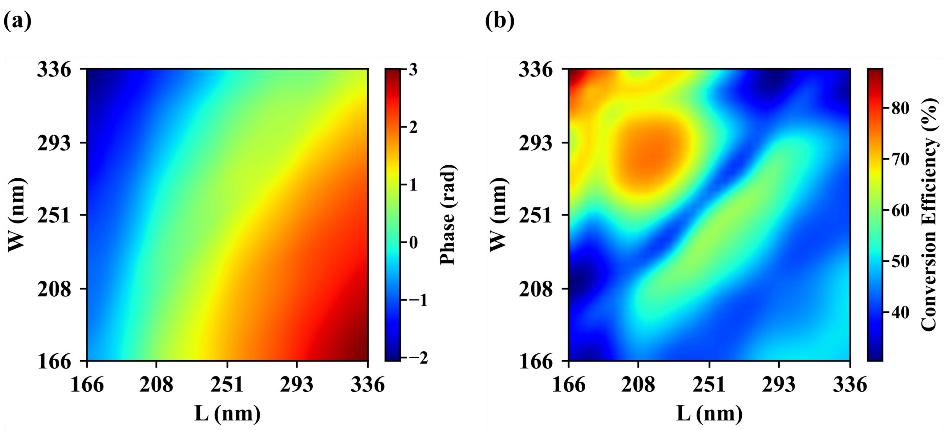

Figure S4. (a) Phase and (b) polarization conversion efficiency distributions of meta-atoms with length **L** = 176-336 nm and width **W** = 166-326 nm at a rotation angle **θ** = 0°.

Supplementary Note 6: Original model and its simulation results

This section presents the simulation results of the original model. Figure S5a shows the schematic diagram of the meta-atom and the overall layout of the metalens. Figure S5b presents the normalized in-plane intensity distribution of the achromatic metalens at each sampled wavelength, where the white dashed lines mark the actual focal length positions corresponding to the five wavelengths. As observed from the figure, the focal length positions remain nearly unchanged with increasing wavelength, indicating excellent achromatic focusing performance of the metalens. Figure S5c shows the electric field intensity distribution at the focal plane under different wavelengths. The results demonstrate that the focal spots at all wavelengths maintain good symmetry without obvious morphological distortion, verifying the metalens' excellent focusing capability. In Figure S5d, a comparative analysis between the normalized intensity curves (colored solid lines) of the horizontal cross-section of the focal plane and the ideal Airy function (black dashed line) reveals that the intensity distribution of the achromatic metalens along the x-axis is highly consistent with the theoretical diffraction limit, and the focal symmetry remains at an ideal level. The focal length variation of the achromatic metalens is shown in Figure S5e. The focal length varies from 112.58 μm to 116.56 μm, with a range of only 3.98 μm. The maximum deviation is less than 2% of the designed focal length within the entire designed wavelength range. Figure S5f shows the focusing efficiency at each wavelength, defined as the ratio of the focal power (three times the FWHM) to the total incident beam power. The simulation results indicate an average focusing efficiency of approximately 42.13%. Figure S5g presents a comparison between the full width at half maximum (FWHM) and the diffraction limit. The calculated FWHM ranges from 5.42λ to 5.88λ, which is close to the theoretical diffraction limit of $\frac{\lambda}{2\mathrm{NA}} = 5.75\lambda$. This indicates that the focal spot diameter is effectively controlled within the operating wavelength range.

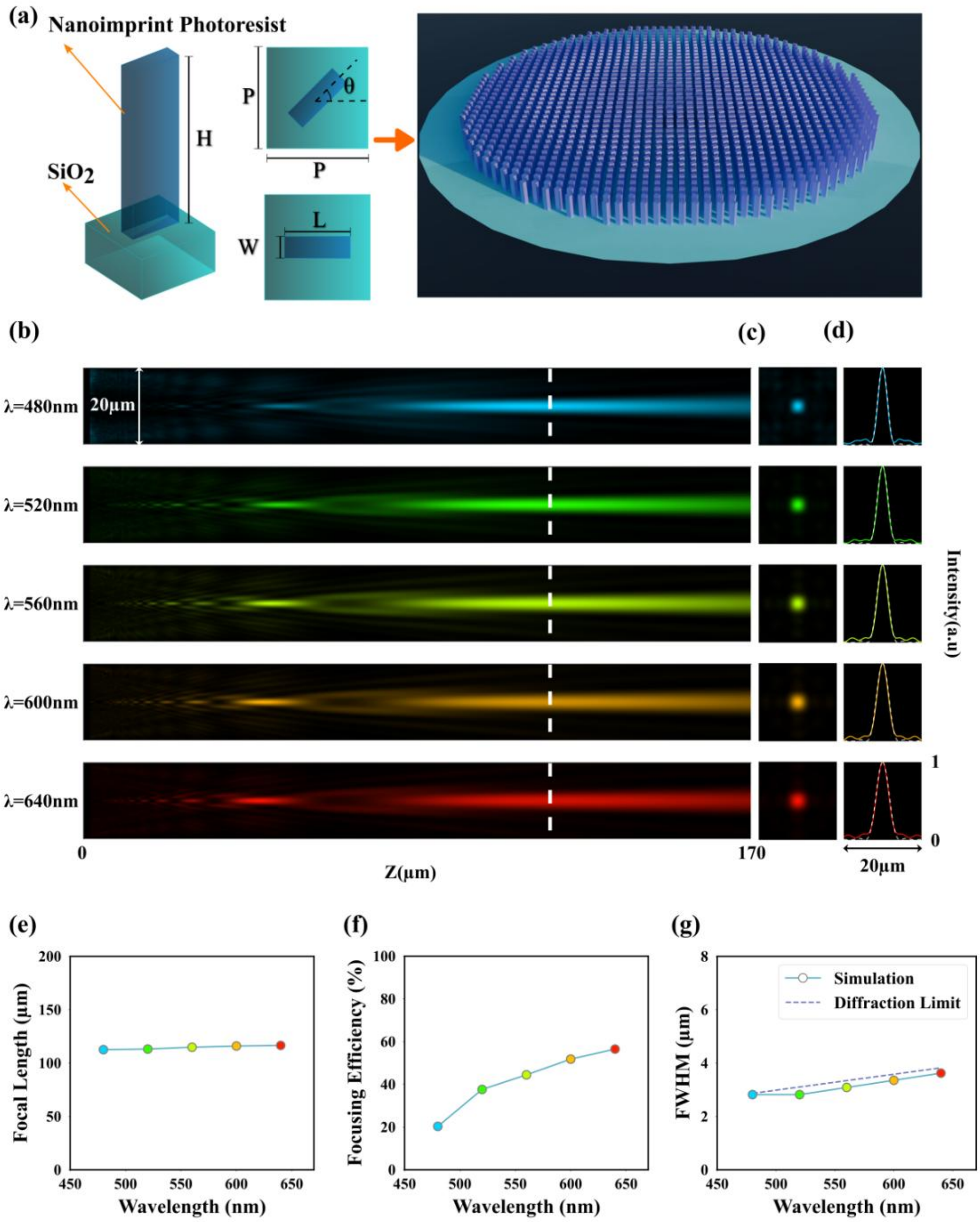

Figure S5. Simulation model and results. (a) Schematic diagram of model construction. Simulation results of the metalens in the 480–640 nm wavelength range, especially for the five sampled wavelengths: (b) Normalized intensity distribution in x-z plane, where the white dashed lines mark the actual focal length positions; (c, d) Normalized intensity distribution and curves of the cross-sections (colored solid lines) and the ideal Airy function (white dashed lines), respectively; (e) Simulated focal lengths; (f) Simulated focusing efficiencies; (g) Comparison between the simulated FWHM (blue solid line) and the diffraction limit (purple dashed line).

Supplementary Note 7: Optical characteristics of the metalens

Table S2 presents the simulated (original model and corrected model) and measured optical characteristics of the metalens, including focal length, focusing efficiency, and FWHM. The arithmetic mean (AM) and standard deviation of the focal length, as well as AM of the focusing efficiency, are also provided.

Table S2. Optical characteristics of the metalens (Unit: μm)

	Wavelength	**480 nm**	**520 nm**	**560 nm**	**600 nm**	**640 nm**	**AM**	**SD**
Focal Length	Original Model (Sim.)	112.58	113.14	114.85	115.99	116.56	114.62	1.74
	Corrected Model (Sim.)	115.42	114.85	115.42	116.56	116.56	115.76	0.76
	Exp.	114.00	115.00	116.00	117.00	116.00	115.60	1.14
Focusing Efficiency	Original Model (Sim.)	20.31%	37.62%	44.44%	51.80%	56.50%	42.13%	
	Corrected Model (Sim.)	23.98%	37.19%	44.86%	50.66%	56.31%	42.60%	
	Exp.	29.33%	25.70%	33.57%	30.81%	35.37%	30.96%	
FWHM	Original Model (Sim.)	2.82	2.82	3.09	3.36	3.62		
	Corrected Model (Sim.)	3.09	3.09	3.09	3.36	3.62		
	Horizontal (Exp.)	3.71	3.02	3.54	3.54	3.71		
	Vertical (Exp.)	3.10	3.45	3.54	3.36	3.62		

Supplementary Note 8: Process flow of the metalens

Figure S6 shows the process flow illustration of the metalens, including the process flow of master fabrication, working stamp fabrication, and nanoimprint lithography (NIL). For detailed information, please refer to the Materials and Methods in the main text.

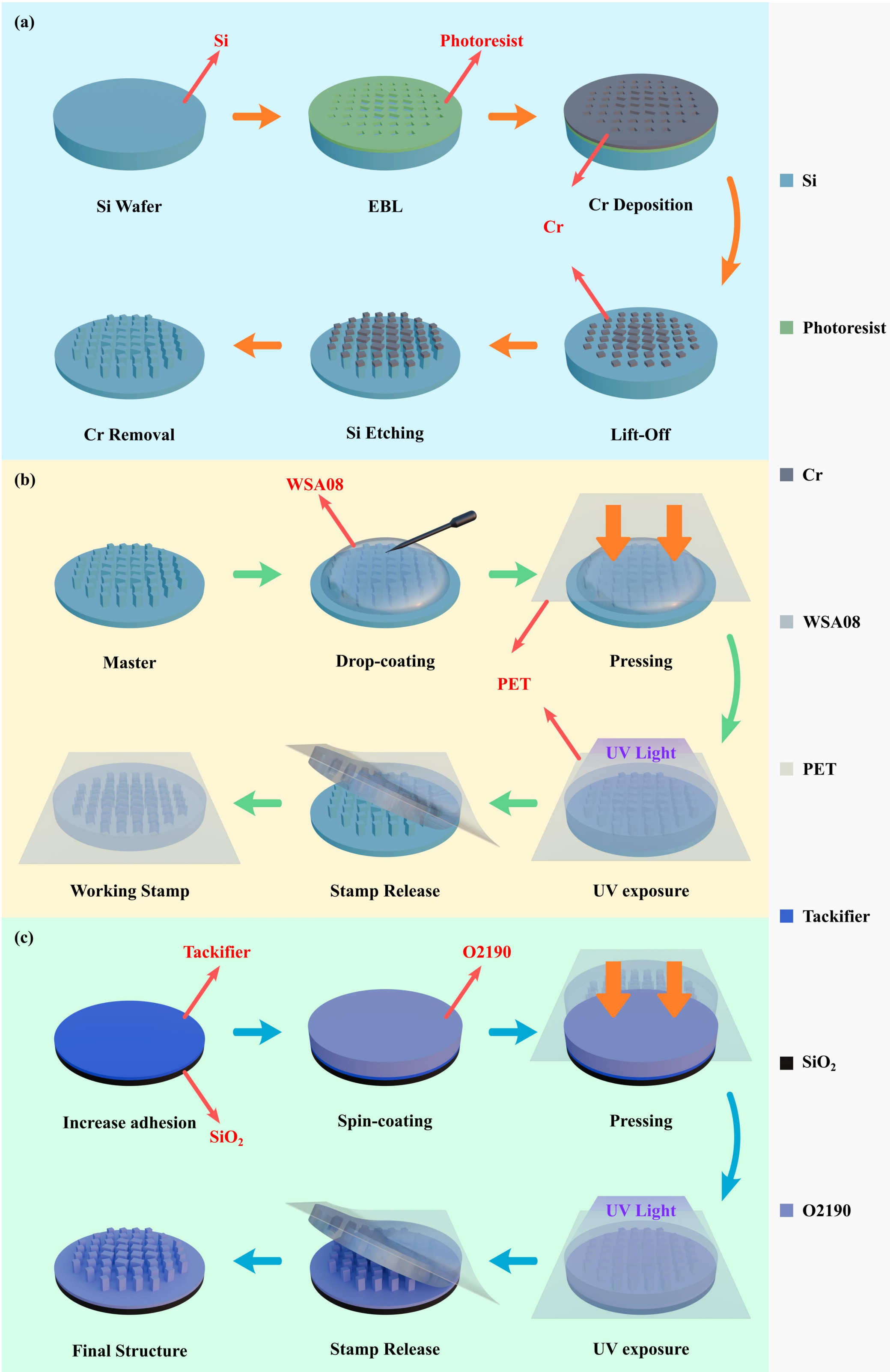

Figure S6. Process flow illustration. (a) Process flow of the master fabrication. (b) Process flow of the working stamp fabrication. (c) Process flow of Nanoimprint lithography (NIL).

Supplementary Note 9: Dimensional measurement and shrinkage rate analysis of meta-atoms

To analyze the structural fidelity induced by each process step, ImageJ (an image analysis software) was used to measure the critical dimensions of meta-atoms in detail from SEM and FIB-SEM images. Due to the certain sidewall tilt angle of the fabricated meta-atoms, the half-height width (W_{Half}), half-height length (L_{Half}), and height (H) were selected as characteristic parameters to analyze the shrinkage rate, which can accurately reflect the change in their actual volume (i.e., equivalent refractive index). The specific measurement and statistical methods are referred to in the Materials and Methods of the main text.

For the lateral shrinkage rate, front-view SEM measurements and dimensional analysis were conducted on 30 meta-atoms in five different regions of the metalens. The numbered SEM images of the master mold, NIL sample, and the other three positions of the metalens are presented in Figures S7, S8, and S9, respectively. Using ImageJ software, W_{Top}, W_{Bottom}, L_{Top}, and L_{Bottom} of each meta-atom were measured one by one, and W_{Half}, L_{Half}, and the corresponding shrinkage rates were calculated; the relevant data are summarized in Tables S3, S4, and S5. The results show that the lateral shrinkage rates of all meta-atoms are no more than 5.19%.

For the vertical shrinkage rate, the heights of 10 meta-atoms were measured and their shrinkage rates calculated, with the numbered image and measurement data provided in Figure S10 and Table S6, respectively; all measured vertical shrinkage rates are no more than 4.87%.

Statistical analysis of the 30 meta-atoms from five different positions shows that the average width shrinkage rate ($W_{Shrinkage}$) is 2.23% ± 1.98%, the average length shrinkage rate ($L_{Shrinkage}$) is 1.87% ± 1.76%, and the average height shrinkage rate ($H_{Shrinkage}$) is 3.47% ± 1.38%. Most shrinkage rates are controlled within 5%, which is basically consistent with the expected target of material optimization.

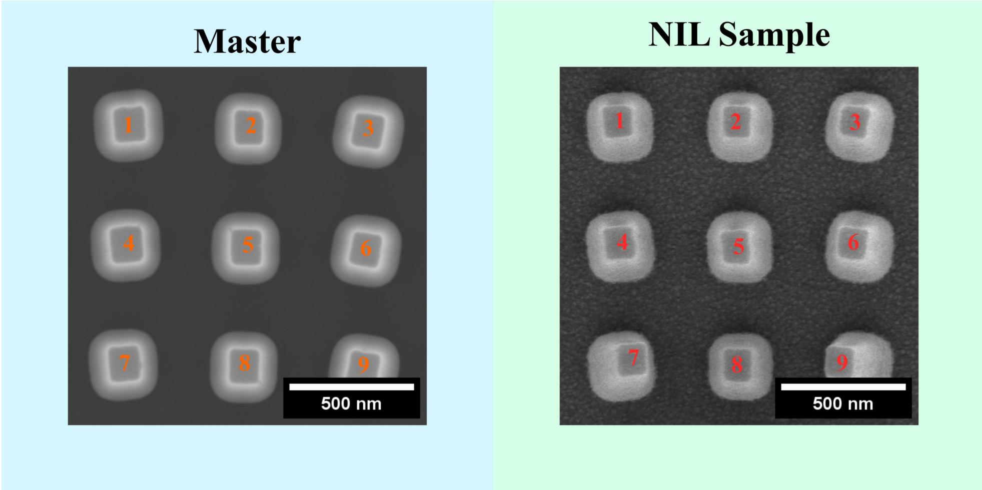

Figure S7. SEM image of meta-atoms at the edge position of the metalens

Table S3. Meta-atom dimensions at the edge of the metalens (Unit: nm)

Number	Sample	W_{Top}	W_{Bottom}	W_{Half}	Shrinkage	L_{Top}	L_{Bottom}	L_{Half}	Shrinkage
1	Master	124.97	269.56	197.26	4.97%	142.22	289.03	215.62	5.00%
	NIL Sample	112.76	262.17	187.47		125.73	283.96	204.85	
2	Master	113.68	258.55	186.12	0.30%	129.20	278.67	203.94	0.84%
	NIL Sample	115.56	255.56	185.56		128.89	275.57	202.23	
3	Master	117.29	274.67	195.98	4.88%	129.44	271.52	200.48	3.21%
	NIL Sample	113.70	259.14	186.42		112.20	275.89	194.04	
4	Master	115.58	271.12	193.35	1.25%	140.02	277.79	208.90	0.38%
	NIL Sample	120.51	261.36	190.94		134.24	281.98	208.11	
5	Master	110.00	264.06	187.03	2.48%	130.11	278.13	204.12	1.25%
	NIL Sample	106.76	258.02	182.39		127.15	275.99	201.57	
6	Master	115.11	284.49	199.80	4.88%	128.27	285.73	207.00	4.42%
	NIL Sample	111.67	268.45	190.06		114.40	281.31	197.85	
7	Master	123.44	270.11	196.78	4.95%	137.80	283.45	210.62	4.97%
	NIL Sample	115.90	258.18	187.04		131.58	268.74	200.16	
8	Master	113.92	265.33	189.63	5.12%	132.98	276.58	204.78	2.87%
	NIL Sample	109.91	249.93	179.92		135.56	262.23	198.90	
9	Master	118.69	271.44	195.07	4.98%	123.97	269.55	196.76	1.76%
	NIL Sample	118.67	252.03	185.35		118.80	267.79	193.29	

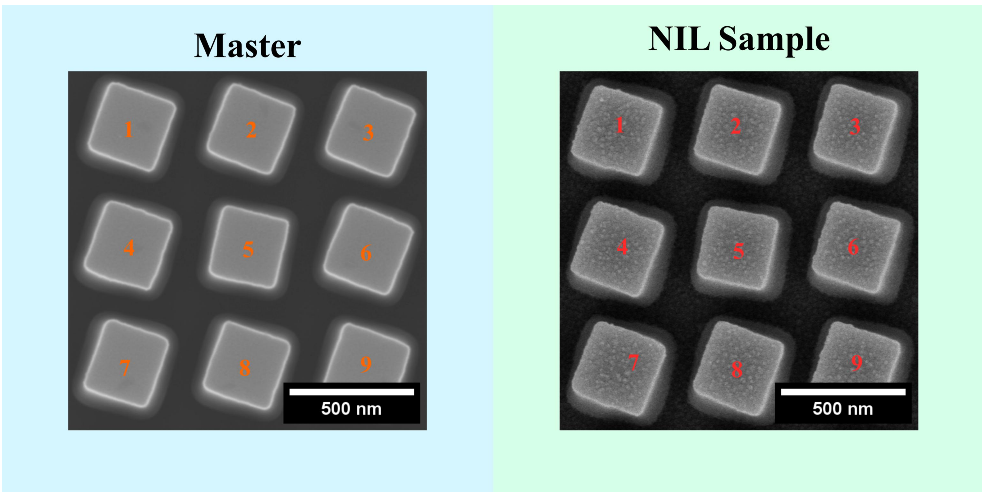

Figure S8. SEM image of meta-atoms at the central position of the metalens

Table S4. Meta-atom dimensions at the center of the metalens (Unit: nm)

Number	Sample	W_{Top}	W_{Bottom}	W_{Half}	Shrinkage	L_{Top}	L_{Bottom}	L_{Half}	Shrinkage
1	Master	276.25	381.58	328.91	0.56%	276.25	381.82	329.03	0.03%
	NIL Sample	272.34	381.80	327.07		276.13	381.76	328.94	
2	Master	275.24	385.46	330.35	4.08%	289.74	393.01	341.38	4.37%
	NIL Sample	265.41	368.31	316.86		279.77	373.12	326.45	
3	Master	269.98	391.21	330.60	4.34%	277.79	385.01	331.40	1.19%
	NIL Sample	263.55	368.95	316.25		275.71	379.17	327.44	
4	Master	269.26	373.18	321.22	0.27%	285.36	383.13	334.25	0.09%
	NIL Sample	265.23	375.47	320.35		285.26	382.64	333.95	
5	Master	263.02	370.29	316.66	0.00%	274.34	383.98	329.16	0.51%
	NIL Sample	264.25	369.08	316.67		276.12	378.82	327.47	
6	Master	272.36	383.39	327.87	0.05%	283.51	389.14	336.33	0.14%
	NIL Sample	272.31	383.14	327.72		283.26	388.47	335.86	
7	Master	254.58	373.86	314.22	0.44%	289.74	388.84	339.29	0.01%
	NIL Sample	254.35	371.32	312.83		288.91	389.57	339.24	
8	Master	274.92	384.08	329.50	4.97%	283.20	380.72	331.96	5.19%
	NIL Sample	262.51	363.77	313.14		267.34	362.11	314.73	
9	Master	275.50	376.70	326.10	0.34%	285.31	383.00	334.16	0.02%
	NIL Sample	270.23	379.73	324.98		282.88	385.27	334.08	

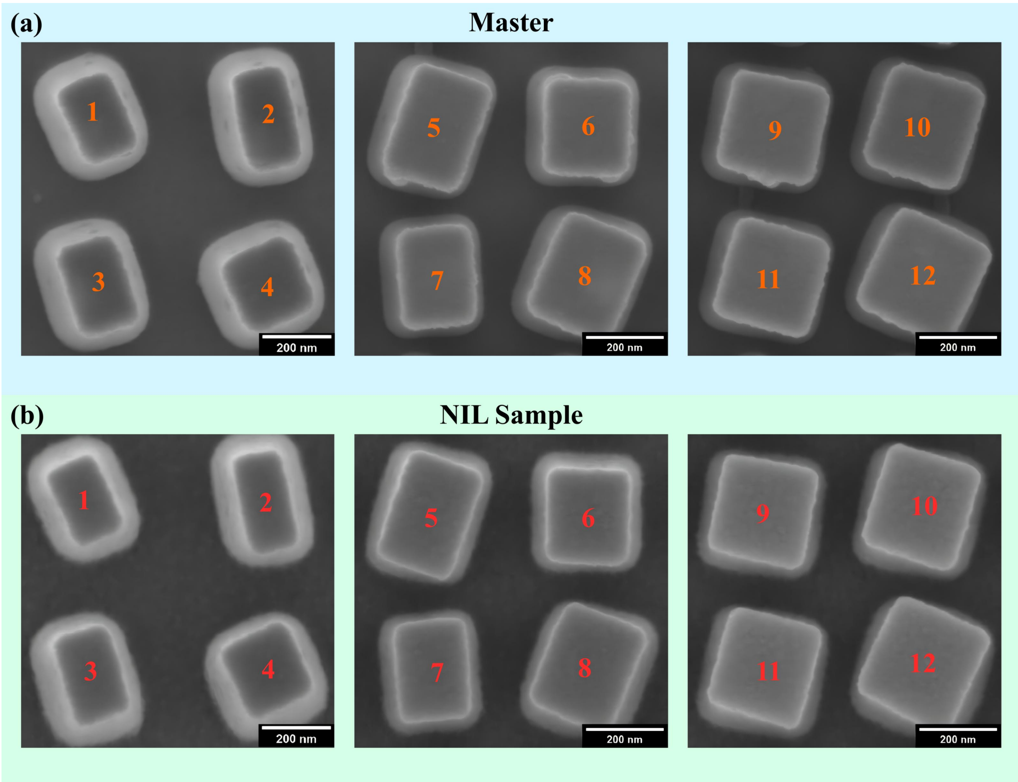

Figure S9. SEM images of meta-atoms at three other positions of the metalens (neither central nor edge regions)

Table S5. Meta-atom dimensions at three other positions of the metalens (neither central nor edge regions) (Unit: nm)

Number	Sample	W_{Top}	W_{Bottom}	W_{Half}	Shrinkage	L_{Top}	L_{Bottom}	L_{Half}	Shrinkage
1	Master	169.13	287.43	228.28	3.60%	247.08	361.06	304.07	4.50%
	NIL Sample	158.51	281.63	220.07		230.48	350.28	290.38	
2	Master	164.51	279.13	221.82	4.05%	294.86	402.48	348.67	1.44%
	NIL Sample	153.77	271.90	212.84		294.83	392.44	343.64	
3	Master	182.22	295.35	238.79	2.37%	275.90	382.61	329.26	1.15%
	NIL Sample	174.21	292.03	233.12		271.80	379.13	325.47	
4	Master	222.39	334.43	278.41	4.27%	242.10	349.90	296.00	3.54%
	NIL Sample	208.95	324.10	266.52		230.00	341.04	285.52	
5	Master	211.95	283.38	247.67	4.11%	294.96	361.40	328.18	0.80%
	NIL Sample	203.59	271.41	237.50		290.96	360.13	325.55	
6	Master	225.11	292.94	259.03	3.27%	243.75	307.26	275.51	0.50%
	NIL Sample	213.41	287.70	250.56		241.60	306.67	274.14	
7	Master	198.68	264.67	231.68	4.26%	261.87	313.06	287.47	4.15%
	NIL Sample	187.29	256.35	221.82		249.89	301.19	275.54	
8	Master	233.26	307.89	270.57	2.04%	289.74	346.95	318.34	3.60%
	NIL Sample	229.92	300.17	265.04		276.17	337.57	306.87	
9	Master	252.44	315.49	283.97	3.74%	256.07	323.79	289.93	4.13%
	NIL Sample	245.11	301.59	273.35		238.47	317.44	277.96	
10	Master	256.70	317.88	287.29	3.43%	276.94	332.54	304.74	5.12%
	NIL Sample	243.43	311.43	277.43		261.86	316.41	289.14	
11	Master	257.67	318.12	287.90	3.62%	265.19	322.25	293.72	5.17%
	NIL Sample	246.22	308.76	277.49		248.82	308.21	278.52	
12	Master	272.24	334.11	303.17	1.15%	286.51	347.65	317.08	3.82%
	NIL Sample	268.41	330.94	299.67		279.27	330.66	304.96	

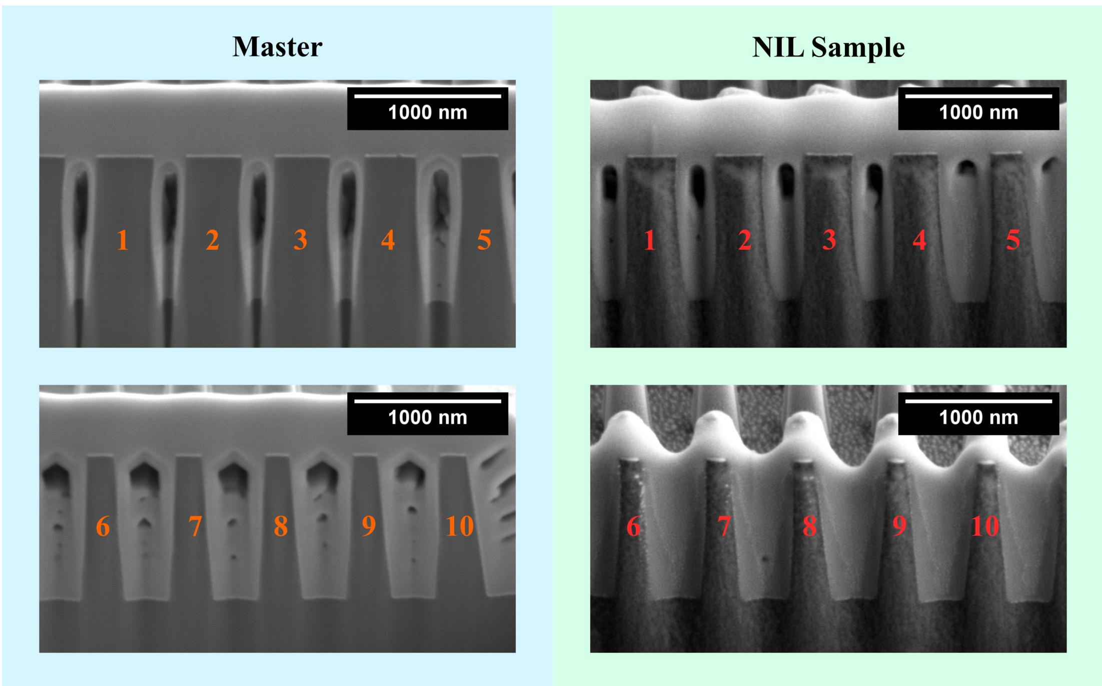

Figure S10. FIB-SEM images of meta-atoms at the central and edge positions of the metalens

Table S6. Meta-atom heights at the central and edge positions of the metalens (Unit: nm)

Number	H		$H_{Shrinkage}$
	Master	NIL Sample	
1	964.45	917.50	4.87%
2	965.72	918.77	4.86%
3	966.99	920.04	4.86%
4	968.26	921.31	4.85%
5	969.53	922.58	4.84%
6	969.53	949.23	2.09%
7	970.80	950.49	2.09%
8	972.07	951.76	2.09%
9	973.34	953.03	2.09%
10	974.61	954.30	2.08%

Supplementary Note 10: Comparison of designed meta-atom Dimensions and measured dimensions of the NIL sample

To compare the dimensional deviation of meta-atoms between the fabricated NIL Sample and the Original Model, the average values of the NIL Sample from Tables S3, S4 and S5 were taken as its dimensions. Figure S7 presents the comparison between the designed meta-atom dimensions and the measured dimensions of the NIL Sample, including both the edge and central regions of the metalens.

Table S7. Comparison of designed meta-atom dimensions and measured dimensions of the NIL sample (Unit: nm)

Area	**Edge**			**Center**		
Parameter	W_{Half}	L_{Half}	**H**	W_{Half}	L_{Half}	**H**
Design	166.00	186.00	1000.00	321.00	331.00	1000.00
NIL Sample	182.29	200.90	951.76	317.39	322.55	920.04
Deviation	+16.29	+14.90	-48.24	-3.61	-8.45	-79.96

Supplementary Note 11: Measured focal lengths of the metalens

For the optical characterization of the fabricated metalens, the focal length was measured five times at five characteristic wavelengths, as shown in Figure S11 and Table S8. Data points in the figure represent the arithmetic mean (AM) of the measurements, and error bars represent the corresponding standard deviation (SD).

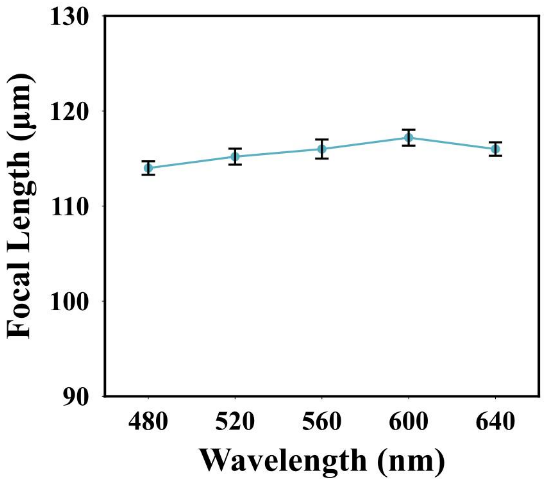

Figure S11. Measured focal lengths of the metalens at different wavelengths, where data points represent the average of five repeated measurements and error bars denote the standard deviation.

Table S8. Focal length data of the metalens at each wavelength from five measurements, along with their average values and standard deviations.

Wavelength	480 nm	520 nm	560 nm	600 nm	640 nm
	114.00	115.00	116.00	117.00	116.00
	113.00	116.00	117.00	118.00	117.00
Focal Length	115.00	115.00	115.00	118.00	115.00
	114.00	114.00	117.00	116.00	116.00
	114.00	116.00	115.00	117.00	116.00
AM	114.00	115.20	116.00	117.20	116.00
SD	0.71	0.84	1.00	0.84	0.71

Supplementary Note 12: Corrected model and its simulation results

This section presents the simulation results of the corrected model. Figure S12a shows the schematic diagram of the corrected meta-atom and the overall layout of the metalens. The simulation results of the original and corrected models show no significant difference (see Table S2), which indicates that our metalens design has high error tolerance.

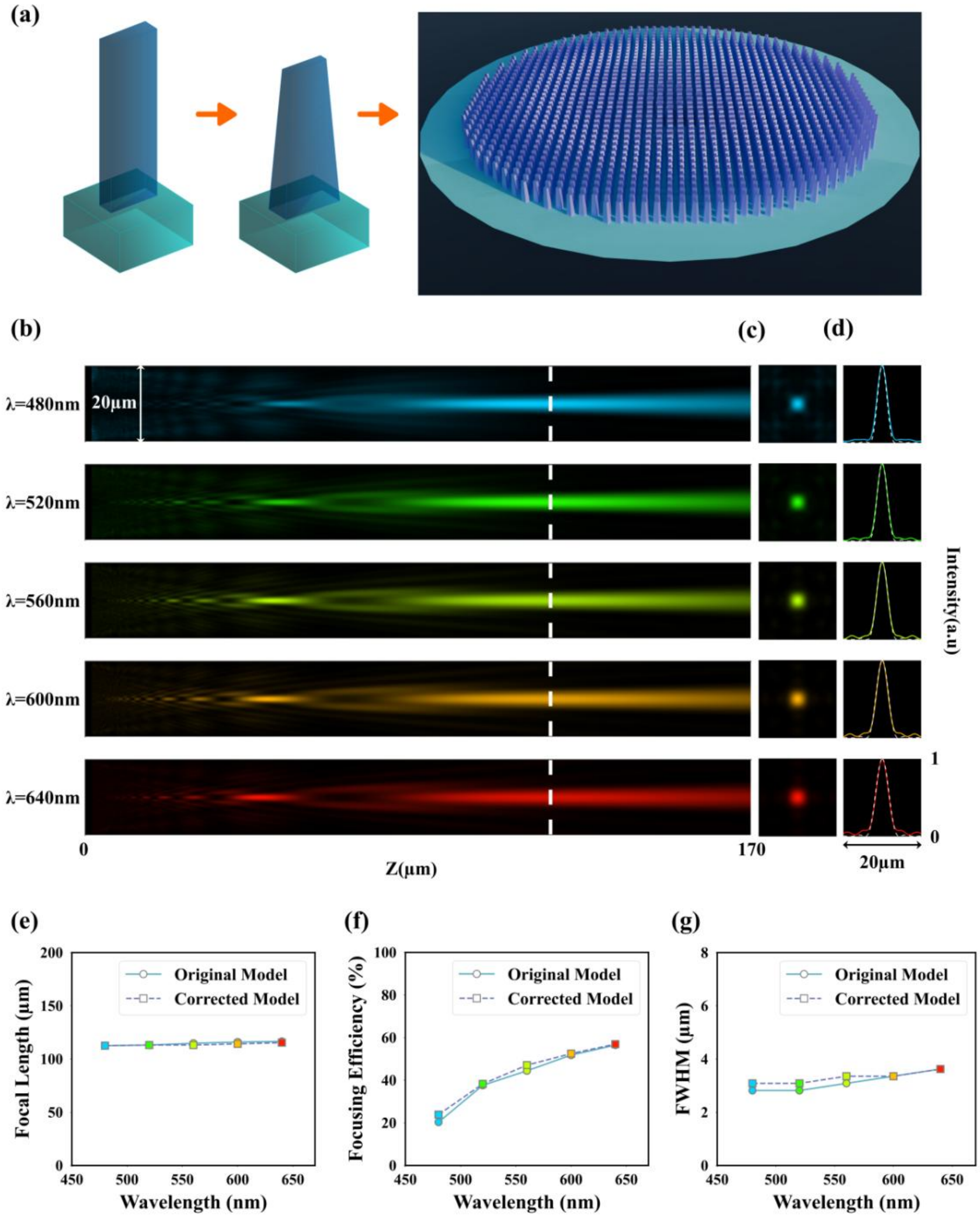

Figure S12. Corrected metalens model and its simulation results. (a) Schematic diagram of the modified model construction. Simulation results of the modified metalens within the 480–640 nm wavelength range, with a focus on five sampled wavelengths: (b) Normalized intensity distribution in the x-z plane, where white dashed lines indicate the actual focal length positions; (c, d) Normalized intensity distribution and cross-sectional intensity curves (colored solid lines), respectively, with the ideal Airy function shown as white dashed lines; (e) Comparison of simulated focal lengths between the original model (circular markers) and the corrected model (square markers); (f) Simulated focusing efficiencies of the original model (circular markers) and the corrected model (square markers); (g) Comparison of simulated full width at half maximum (FWHM) between the original model (circular markers) and the corrected model (square markers).

Supplementary Note 13: Analysis of factors causing discrepancy between simulated and measured focusing efficiency

Noting the mismatch between simulated and measured focusing efficiency in Figure 4f, we conducted a quantitative analysis of potential influencing factors, including meta-atom dimension error, residual layer, surface roughness, imprint depth nonuniformity, systematic phase errors and measurement errors.

Table S9. Simulated focusing efficiency with various fabrication-induced errors

Wavelength	480 nm	520 nm	560 nm	600 nm	640 nm
Original model	20.31%	37.62%	44.44%	51.80%	56.50%
Varying meta-atom dimensions	23.85%	38.28%	47.09%	52.51%	56.93%
With residual layer	23.58%	37.00%	44.66%	50.64%	56.13%
Surface roughness (0.001 μm)	23.58%	36.99%	44.66%	50.63%	56.13%
Actual height variation	23.98%	37.19%	44.86%	50.66%	56.31%
Rotation angle error of ±10°	23.72%	36.82%	44.53%	50.33%	55.99%

Original model: It refers to the ideal model without any errors introduced.

Varying meta-atom dimensions: Measured from Figure 3, the meta-atom size decreases by 6.03 nm at the center and increases by 15.60 nm at the edge. This error was introduced into the original model. Simulation results show its influence on focusing efficiency is negligible, indicating it is not the main cause of the discrepancy (see Table S9).

With residual layer: Based on actual process tests and FIB-SEM characterization, a ~2 μm thick residual layer of nanoimprint photoresist exists on the metalens substrate. Simulations demonstrate its negligible impact on focusing efficiency, so it is not the main cause of the discrepancy (see Table S9).

Surface roughness: AFM characterization of the actual sample shows a RMS surface roughness of ~0.001 μm. Introducing this roughness into the corrected model, simulations reveal its negligible influence on focusing efficiency, excluding it as the main cause (see Table S9).

Imprint depth nonuniformity: FIB-SEM cross-sectional images (see Figure S10) and ImageJ statistics (see Table S6) show the actual meta-atom height ranges from 920.04 nm to 951.76 nm. The corrected model introduced these actual heights. Simulations confirm its negligible effect, so it is not the primary cause (see Table S9).

Systematic phase errors: Considering the imperfect matching between the actual meta-atom rotation angle and the designed value during imprinting, a ±10° random rotation error was introduced into all meta-atoms in the corrected model. Simulations show this process error has a relatively small overall impact on focusing efficiency (see Table S9).

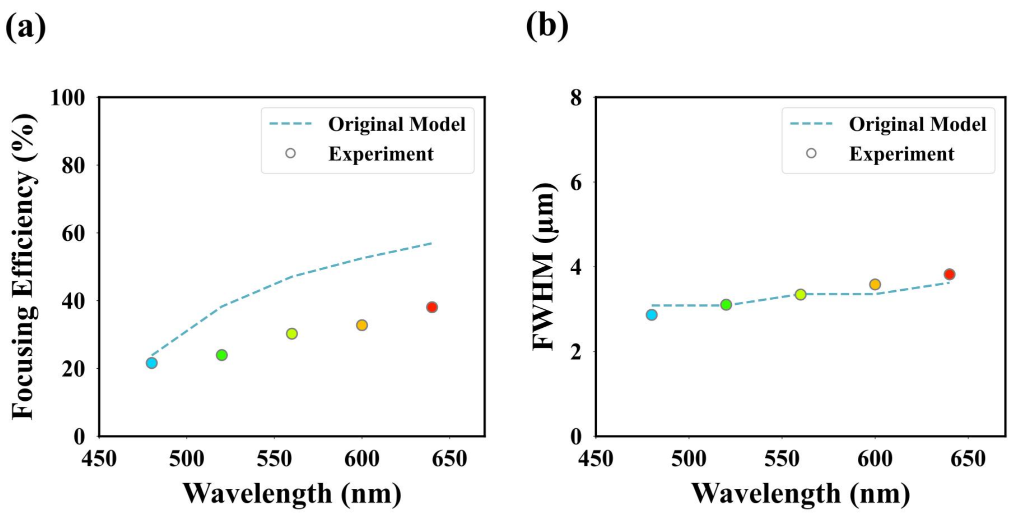

Figure S13. Measured and corrected (a) focusing efficiency and (b) FWHM with measurement errors

Table S10. Measured and corrected FWHM and focusing efficiency with measurement errors

Wavelength		480 nm	520 nm	560 nm	600 nm	640 nm
FWHM (μm)	Original measured	3.41	3.24	3.54	3.45	3.67
	Corrected	2.87	3.10	3.34	3.58	3.82
Focusing Efficiency	Original measured	29.33%	25.70%	33.57%	30.81%	35.37%
	Corrected	21.62%	23.96%	30.27%	32.77%	38.07%

Measurement errors: When extracting and comparing the FWHM of metalens focal spots at different wavelengths, systematic errors in measured intensity distribution arise from differences in camera quantum efficiency, responsivity, and exposure parameters. Data normalization included calibration of intensity distribution weighted by camera spectral response, background noise subtraction, and baseline correction for each focal spot image. This eliminated measurement system-induced deviations, ensuring reliable comparison of FWHM and focusing efficiency across wavelengths. After correction, the measured FWHM and focusing efficiency trends agree well with simulations, but the measured focusing efficiency is still lower than the simulated value. (see Figure S13 and Table S10).

In summary, we attribute the lower measured focusing efficiency relative to simulations to the following possible reasons: (1) Limited resolution of the detection system. (2) Ambient stray light and background noise. (3) Polarization mismatch in the actual optical path.